JGR Planets

RESEARCH ARTICLE
10.1029/2024JE008620

Key Points:

- For the first time, NOMAD/UVIS simultaneously monitors both the NO UV and O_2 visible nightglow in the Mars southern winter atmosphere
- The NO emitting layer is consistently located ∼10 km above the O_2 nightglow layer (∼55 and ∼45 km, respectively)
- Brightness is overall well predicted but the altitude difference between the two polar emission layers is overestimated by the MPCM v6.1 model

Correspondence to:
L. Soret,
lauriane.soret@uliege.be

Citation:
Soret, L., González-Galindo, F., Gérard, J.-C., Thomas, I. R., Ristic, B., Willame, Y., et al. (2024). Ultraviolet NO and visible O_2 nightglow in the Mars southern winter polar region: Statistical study and model comparison. *Journal of Geophysical Research: Planets*, *129*, e2024JE008620. https://doi.org/10.1029/2024JE008620

Received 17 JUL 2024
Accepted 10 NOV 2024

Author Contributions:
Conceptualization: L. Soret, J.-C. Gérard
Funding acquisition: B. Hubert
Methodology: L. Soret
Project administration: I. R. Thomas, A. C. Vandaele, B. Hubert, M. R. Patel
Software: L. Soret
Visualization: L. Soret
Writing – original draft: L. Soret, J.-C. Gérard
Writing – review & editing: L. Soret, J.-C. Gérard

Ultraviolet NO and Visible O_2 Nightglow in the Mars Southern Winter Polar Region: Statistical Study and Model Comparison

L. Soret[1], F. González-Galindo[2], J.-C. Gérard[1], I. R. Thomas[3], B. Ristic[3], Y. Willame[3], A. C. Vandaele[3], B. Hubert[1], F. Lefèvre[4], F. Daerden[3], and M. R. Patel[5]

[1]LPAP, STAR Institute, Université de Liège, Liège, Belgium, [2]Instituto de Astrofísica de Andalucía—CSIC, Granada, Spain, [3]Royal Belgian Institute for Space Aeronomy, Brussels, Belgium, [4]LATMOS, Paris, France, [5]School of Physical Sciences, The Open University, Milton Keynes, UK

Abstract The Mars NO and the O_2 nightglow are produced by the recombination of atoms produced on the dayside by photodissociation and transported to the nightside. These emissions are tracers of the summer to winter pole dynamics in the upper Mars atmosphere. The UV-visible (UVIS) channel of the Nadir and Occultation for MArs Discovery (NOMAD) spectrometer onboard Trace Gas Orbiter (TGO) is the first instrument able to simultaneously monitor both nightglow emissions. Observations by NOMAD/UVIS during the first part of the Martian year show that both the NO and O_2 nightglow emissions are enhanced near the southern winter pole. Their mean brightnesses are 15 and 108 kR, respectively. These nightglow emissions generally occur between 30 and 60 km, the NO emitting layer being consistently located ∼10 km higher than the O_2 nightglow layer. Numerical simulations with the Mars Planetary Climate Model (MPCM, v6.1) properly reproduce the nightglow brightness but tend to overestimate the NO peak altitude by ∼10 km. These results suggest that the atomic oxygen density is correctly predicted by the model but that the nitrogen density altitude distribution might not be properly modeled.

Plain Language Summary Nightside emissions of the Martian upper atmosphere are excited by the recombination of atoms created on the dayside. For the first time, the NO ultraviolet emission and the O_2 visible emission have been observed simultaneously with the UV-visible (UVIS) channel of the Nadir and Occultation for MArs Discovery (NOMAD) spectrometer onboard Trace Gas Orbiter (TGO). They are used as tracers of the atmospheric dynamics to demonstrate the summer to winter pole circulation that governs the Mars upper atmosphere. We show that the two nightglow layers occur between 30 and 60 km and that they are separated by ∼10 km. We compare our results with simulations from the Mars Planetary Climate Model. Simulations manage to properly reproduce the nightglow brightness but tend to overestimate the NO peak altitude by ∼10 km. These results suggest that the atomic oxygen density is correctly predicted by the model but that the altitude distribution of the nitrogen density might not be properly modeled.

1. Introduction

1.1. The NO Nightglow

Nightglow observations have proven to be a powerful tool to remotely probe the composition and dynamics of planetary atmospheres. The first Mars nightglow observations were made in the ultraviolet (UV) with the Spectroscopy for Investigation of Characteristics of the Atmosphere of Mars (SPICAM) instrument on board Mars Express (Bertaux et al., 2005). They correspond to the emission of nitric oxide following the two-body recombination of O and N atoms produced by the photodissociation of CO_2 and N_2 on the dayside with subsequent transport to the nightside. The NO nightglow intensity is therefore proportional to the product of the atomic oxygen and nitrogen densities. This nightglow spectrum is characterized by the presence of the v' = 0 sequence from the δ and γ bands extending between 190 and 270 nm. Further observations from SPICAM (Cox et al., 2008; Gagné et al., 2013; Stiepen et al., 2015) showed that the brightest emission is concentrated at high latitudes (above ∼60°) during the winter periods and shows a peak at lower altitudes in the polar regions, between ∼40 and 80 km. These studies confirmed that the Mars upper atmosphere dynamics is governed by a summer to winter circulation. Gagné et al. (2013) noted that the frequency and magnitude of the NO nightglow show important asymmetries between the northern and the southern hemispheres. They found no detection at high latitudes during equinox

conditions, while model predictions indicate that it should then be most intense owing to a large-scale circulation with two descending branches at the poles.

Extensive observations with the Imaging Ultraviolet Spectrograph (IUVS) on board the Mars Atmosphere and Volatile EvolutioN (MAVEN) orbiter provided global coverage of the latitudinal and seasonal NO nightglow using both limb (Stiepen et al., 2017) and nadir spectral images (Schneider et al., 2020). They showed longitudinal structures in the NO brightness associated with planetary waves and tides. Although the general features of the NO nightglow are well reproduced by numerical simulations, it was found that they overestimate the altitude of the peak emission by about 20 km at all latitudes except in the northern polar region.

1.2. The O_2 ($a^1\Delta$) Nightglow

The second emission identified in the Mars nightglow was the O_2 ($a^1\Delta$)→($X^3\Sigma_g$) infrared (IR) atmospheric band at 1.27 μm. The O_2 nightglow is produced by recombination of O atoms produced in the dayside and transported to the nightside, and is thus controlled by the O density distribution and traces atmospheric transport. In this case, the process involved is the three-body recombination O + O + CO_2, in contrast to the two-body O + N source of excited NO molecules, but the transport remains the summer to winter circulation. The O_2 nightglow intensity is proportional to the square of the atomic oxygen density. It was first observed using the OMEGA spectrometer onboard Mars Express by Bertaux et al. (2012). Three limb profiles (two in the South, one in the North) were obtained in the polar night with peak limb brightness at 42–49 km above the areoid, lower than the NO emission layer.

Further limb detections were made by Fedorova et al. (2012) with the SPICAM-Infrared channel at 82–83° S during two seasons (Ls = 111°–120° and Ls = 152°–165°) at altitudes between 38 and 45 km. From the O_2 ($a^1\Delta_g$) nightglow SPICAM data set, it was possible to estimate the density of oxygen atoms at altitudes from 50 to 65 km. It was found to vary from 1.5×10^{11} to 2.5×10^{11} cm^{-3}. Simulations with the Mars Planetary Climate Model (M-PCM, formerly known as Laboratoire de Météorologie Dynamique Mars Global Climate Model, LMD-MGCM initially developed by Forget et al., 1999) of the altitude of the 1.27 μm layer (Lefèvre et al., 2004) showed good agreement with the observations. Simulations confirmed the summer to winter circulation in the Mars upper atmosphere but somewhat overestimated the nadir brightness.

A third set of 1.27 μm observations was provided by the Compact Reconnaissance Imaging Spectral Mapping (CRISM) instrument on the Mars Reconnaissance Orbiter (MRO). Clancy et al. (2012) made extensive limb measurements of the O_2 IR atmospheric nightglow in both polar regions with CRISM between 2009 and 2011. They showed that the emission peak was observed between 70° and 90° at an altitude between 40 and 60 km.

1.3. The O_2 Herzberg II Nightglow

Strong visible O_2 Herzberg II bands corresponding to the $c\ ^1\Sigma_u \rightarrow X\ ^3\Sigma_g$ Herzberg II bands were first observed on the Venus nightside with the visible spectrometer on Venera 9 and 10 by Krasnopolsky (1983), from Pioneer Venus by Bougher and Borucki (1994) and Venus Express by Garcia-Muñoz (2009). It is characterized by the presence of the v' = 0 band sequence between 400 and 600 nm and is expected to occur at the Venus antisolar point, following the subsolar-to-antisolar global circulation. The Venus spectrum from Garcia-Muñoz (2009) will be used as a reference spectrum later in this study (Section 3.1).

The Mars counterpart of this Venusian nightglow was expected since: (a) the photochemical processes involved in the production of the O_2 visible nightglow are similar to those of the O_2 1.27 μm emission; (b) the composition of both the Mars and Venus atmospheres are dominated by CO_2, with O and N as minor species. The Mars O_2 Herzberg II nightglow was first investigated by a spectrometer on board the Soviet probe Mars 5, sensitive between 300 and 800 nm. No O_2 emission exceeding the instrumental threshold was detected in this spectral range on the planet's nightside limb. Model simulations predicted a nadir intensity of 260 R for fall equinox at low latitudes conditions (Krasnopolsky, 2011). Failure to detect the O_2 visible emission might be due to the low spectral sensitivity of previous instruments and to the fact that observations were mostly made during daytime (Gagné et al., 2012).

The O_2 Herzberg II bands have finally been observed on the Mars nightside by Gérard et al. (2024) with the UVIS channel of the NOMAD suite of instruments (Vandaele, López-Moreno, et al., 2018). Its production mechanism is similar to that of the O_2 ($a^1\Delta$) infrared nightglow (see Section 1.2) and its brightness is also proportional to the

square of the atomic oxygen density. The O_2 visible nightglow shows a spectral composition similar to the Venus visible nightglow previously observed by Krasnopolsky (1983), Bougher and Borucki (1994) and Garcia-Muñoz (2009). Positive Mars detections were concentrated in the polar winter regions of both hemispheres, mainly poleward of 65° latitude. Analysis of the relative detection frequency showed that they were grouped between 35 and 59 km with a maximum detection probability at 42 km reaching 76%. The limb brightness ranged between the detection threshold, on the order of a few tens of kilorayleighs, and up to several hundreds of kilorayleighs. The brightest spectrum reached an intensity of 290 kR at 76° N and 41 km altitude. Gérard et al. (2024) showed comparisons of O_2 Herzberg II measured limb intensities with NOMAD/UVIS and modeled brightness using O and CO_2 densities and temperatures extracted from the Mars Climate Database (MCD, Millour et al., 2022). They concluded that the observed intensities and simulations were in fair agreement.

1.4. Goals of the Study

The possibility to simultaneously observe both the O_2 Herzberg II bands and the nitric oxide nightglow by UVIS opens the door to studying the different transport regimes at different altitudes, posing stronger constraints to global climate models.

This study presents the first simultaneous observations of NO and O_2 nightglow in the southern winter hemisphere of Mars. Section 2 concentrates on the NOMAD/UVIS campaign dedicated to the observation of the southern winter pole. The O_2 (Section 3.1) and NO (Section 3.2) nightglow analysis are described in the next sections. Simultaneous observations of the ultraviolet and visible nightside emissions are then compared to model simulations in Section 3.3. Finally, we demonstrate in Section 3.4 that the O_2 Herzberg II visible emission and the O_2 1.27 μm infrared emission share similar properties and can be used interchangeably to monitor the same region of the Mars upper atmosphere.

2. The ExoMars/TGO/NOMAD/UVIS Observations

2.1. The ExoMars/TGO/NOMAD/UVIS Instrument

The Trace Gas Orbiter (TGO) was inserted into a Mars orbit on 19 October 2016, then after aerobraking, was placed into a quasi-circular orbit inclined by 74° at about 400 km to start science operations on 21 April 2018. The NOMAD/UVIS spectrometer (Patel et al., 2017; Vandaele, López-Moreno, et al., 2018, Vandaele, Neefs et al., 2018) can perform limb measurements on the nightside of the planet through the use of special pointing modes; the number varies depending on the orbit geometry and other observations, but typically several observations can be made per week.

The UVIS spectrometer operates between 200 and 650 nm, with a spectral resolution ranging from 1.2 nm at 200 nm to 1.7 nm at 650 nm (Willame et al., 2022). The NO ultraviolet and O_2 visible nightglow can therefore be observed simultaneously. Limb observations have been performed in both the inertial mode (where a range of altitudes of the tangent point is scanned) and the limb tracking mode (the altitude of the tangent point is stabilized during the time of the observation while a latitudinal scan is performed). Acquisition of nightside inertial limb observations began on 13 March 2020 (MY 35, $L_S = 165°$), while nightside limb tracking observations started on 3 February 2021 (MY 35, $L_S = 358°$). In this study, a minimum solar zenith angle (SZA) of 105° at the tangent point location was imposed for the nightside observations.

The data processing pipeline is as follows: (a) removal of the instrumental background and dark current on the CCD frame; (b) correction of the noise from cosmic rays, anomalous and hot pixels; (c) binning of the 81 CCD lines fully illuminated by the desired incoming light to increase the spectrum signal-to-noise ratio; (d) conversion of the count rate into brightness units (kR) based on laboratory measurements obtained during ground-based and in-flight calibration campaigns. Willame et al. (2022) discuss all these calibration steps, together with the uncertainties of the relative instrumental calibration that is estimated to be less than 10%.

2.2. UVIS Dedicated Campaign

Following the discovery of the O_2 Herzberg II nightglow with NOMAD/UVIS (Gérard et al., 2024), a dedicated campaign to monitor this nightglow at high southern winter latitudes was initiated. The present study focuses on the southern winter period between $L_S = 0$ and 180° and all available observations acquired during these conditions have been considered (from 13 March 2020–MY 35 to 4 January 2024–MY 37). With the dedicated

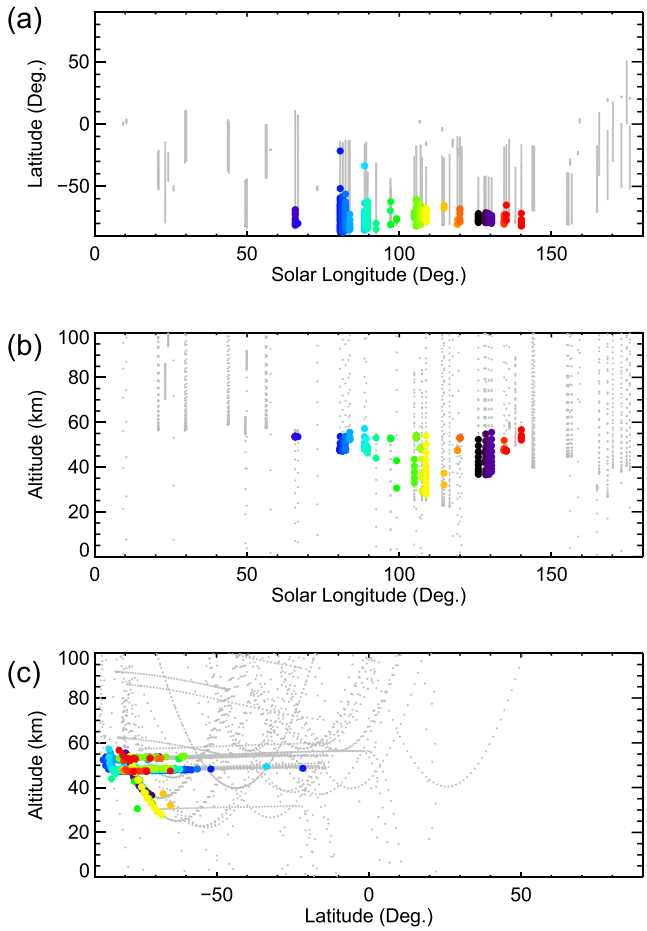

Figure 1. Positive detections ($R > 0.50$) of the O_2 Herzberg II nightglow in the Mars atmosphere between $L_S = 0$ and 180° and between 0 and 100 km (colored dots). The nightglow is mainly detected at high southern latitudes, for altitudes between ∼30 and 60 km. Gray dots represent all the UVIS nightside observations collected between 0 and 100 km, without a clear signature of the O_2 nightglow. To facilitate comparison between panels, detections are color coded according to orbit number (from black during MY 35 to red in MY 37).

campaign, the total number of nightside limb observations acquired between solar longitudes 0 and 180 increased from 35 orbits on 31 January 2022 (MY 36) to 92 orbits on 4 January 2024 (MY 37). The locations of the tangent points of the observations are represented in Figure 1 (both gray and colored dots). With the dedicated campaign, the coverage of the southern winter pole increased both in solar longitude and latitude. Figure 1b shows that most observations were made above 45 km.

3. Results

3.1. The O_2 Nightglow

The entire UVIS nightside limb data set (SZA > 105° and L_S < 180°) was examined to identify O_2 Herzberg II signatures. The methodology was described in Gérard et al. (2024). It consists of calculating the Pearson-R correlation coefficient between each UVIS individual spectrum and the Venus nightglow spectrum (García Muñoz et al., 2009) used as the reference spectrum (see Section 1). The Pearson-R linear correlation coefficient value ranges between 0 (no correlation) and 1 (perfect correlation with the reference spectrum). Only the (0–6) to (0–10) bands are considered to estimate the correlation coefficient. All the available UVIS spectra have been sorted in increasing order according to their Pearson-R correlation coefficient. Then, all spectra have been carefully visually inspected and a threshold was set on the Pearson-R correlation coefficient to ensure that all the spectra above this threshold bear the signature of a real detection. We decided to retain all the spectra with $R > 0.50$ as real O_2 nightglow signatures. These 289 positive detections of the O_2 visible nightglow in the Mars atmosphere are represented with colored dots in Figure 1. The orbit number is color coded from black (MY 35) to red (MY 37). Positive detections are found at high southern latitudes, in agreement with the summer to winter pole atmospheric circulation concept. Parabolas displayed in Figure 3c correspond to inertial limb observations, while horizontal lines are due to limb tracking observations at a constant altitude.

Figure 1 clearly establishes that the Herzberg II nightglow occurs at high winter latitudes in a limited altitude range. In order to improve the statistics, the study will now focus on observations acquired in a restricted southern polar area, with the following criteria: SZA > 105°, solar longitude from 60° to 150°, altitude between 20 and 60 km of altitude and between 50°S and 90°S. The observations of this restricted data set are distributed in altitude according to Figure 2a. Light blue dots represent all the UVIS nightside limb observations matching the criteria. Two peaks clearly appear at ∼48 km and especially at ∼52 km. They are associated with limb tracking observations at these altitudes that considerably increase the number of spectra acquired at these heights. Amongst those observations, 287 positive detections of the O_2 nightglow have been found. The detection threshold remains $R > 0.50$. The dark blue histogram represents the altitude distribution of these O_2 nightglow-positive detections. Again, two peaks clearly appear but that at ∼48 km is now the strongest one. The occurrence rate of the O_2 nightglow altitude is illustrated in green in Figure 2b. It was calculated by dividing the dark blue histogram (positive detections) by the light blue one (all detections) of Figure 2a. The shape of this distribution is completely different. More than 30% of the O_2 signatures were detected between 39 and 52 km. The large values around 30 km should be cautiously considered since they rely on a very limited sample of observations.

Figure 2c shows the brightness distribution of the 287 O_2 nightglow detections. The brightness is estimated using the Venus reference spectrum fit between the (0–6) and (0–10) bands multiplied by 1.33 to account for the rest of the O_2 Herzberg II system (from band 0–5 to 0–13). Limb brightness in the southern hemisphere ranges between 45 and 175 kR, with a mean value of 108 kR. These values are in good agreement with previous measurements and MCD v6.1 simulations (Gérard et al., 2024; Millour et al., 2022). However, note that intensities less than

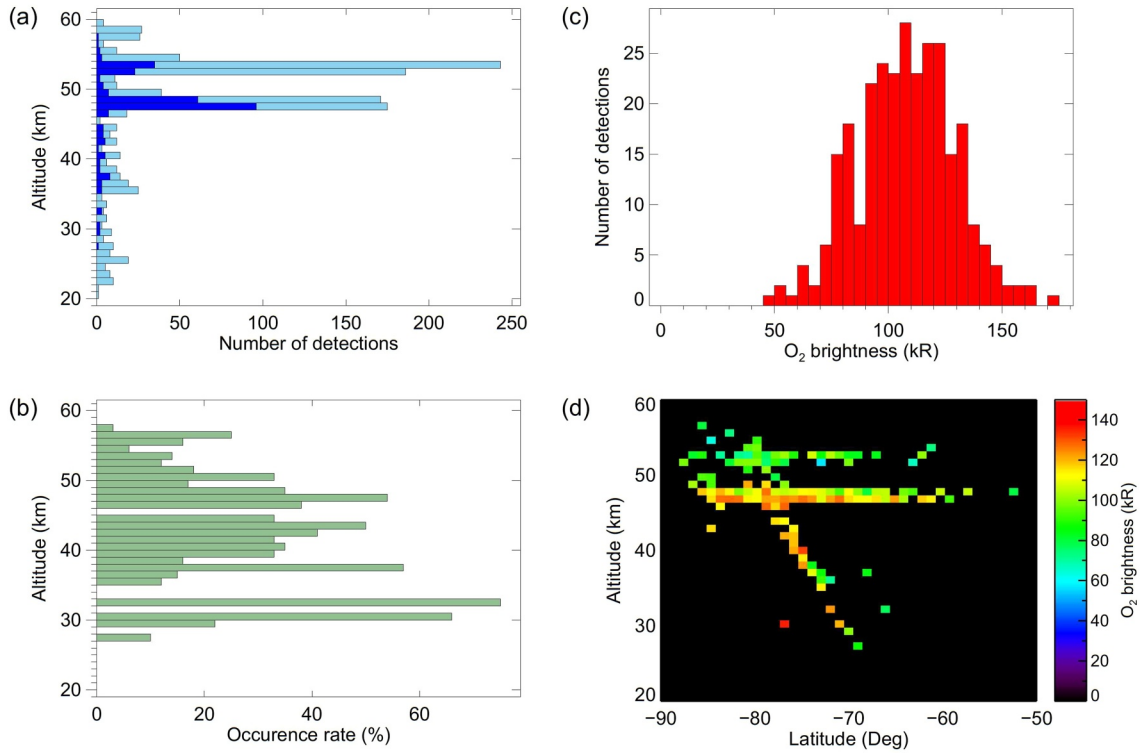

Figure 2. (a) Altitude distribution of the tangent point of the observations. Light blue represents all the UVIS observations matching the following criteria: SZA > 105°, between 60 and 150° of solar longitude, between 20 and 60 km of altitude and between 50°S and 90°S. Dark blue represents positive O_2 detections ($R > 0.50$). (b) Occurrence rate of the O_2 altitude distribution. (c) Brightness distribution. (d) Latitude-altitude map of the O_2 brightness from NOMAD/UVIS nightside limb observations.

45 kR cannot be observed with UVIS due to the limited sensitivity of the instrument. Observed intensities are bright enough to be seen by the naked eye of an astronaut from the ground under clear sky conditions or from an orbiter. According to the Herzberg II spectral distribution, this nightglow is expected to be green, which corresponds to the peak sensitivity of the human eye.

The map of the O_2 brightness displayed in latitude/altitude coordinates (Figure 2d) clearly illustrates that the maximum of the emitting layer is located below 50 km. The latitudinal coverage is sufficient at ∼48 and ∼52 km because of limb tracking observations at those altitudes but could be improved in the future at other altitudes. According to Figure 2d, the actual peak brightness appears to be located below 47 km.

3.2. The NO Nightglow

The NOMAD/UVIS nightside limb database is now examined again, independently from the study presented in Section 3.1. The goal is now to find signatures of the NO ultraviolet nightglow. NOMAD/UVIS allows to observe the δ and γ bands from 200 to 280 nm. The reference spectrum used to calculate the Pearson-R correlation coefficient is a MAVEN/IUVS mean spectrum from Stiepen et al. (2017). Starting a new independent visual inspection of all the available NO spectra, the threshold for the correlation coefficient to select individual UVIS spectra with a reliable NO nightglow signature was set to 0.34. The brightness of the emission was calculated by integrating the MAVEN/IUVS spectrum fitted to the NOMAD/UVIS spectrum. The 435 positive detections of the NO ultraviolet nightglow in the Mars atmosphere found in the NOMAD/UVIS nightside database are represented with colored dots in Figure 3. The orbit number is color coded from black (MY 35) to red (MY 37), independently from Figure 1. As for the O_2 nightglow, the positive NO detections were found at high southern latitudes, in agreement with the MAVEN/IUVS nadir observations and the M-PCM simulations (Schneider et al., 2020). These NOMAD/UVIS data are the first limb observations performed so far poleward of 65°S, between 50° and 150° of solar longitude.

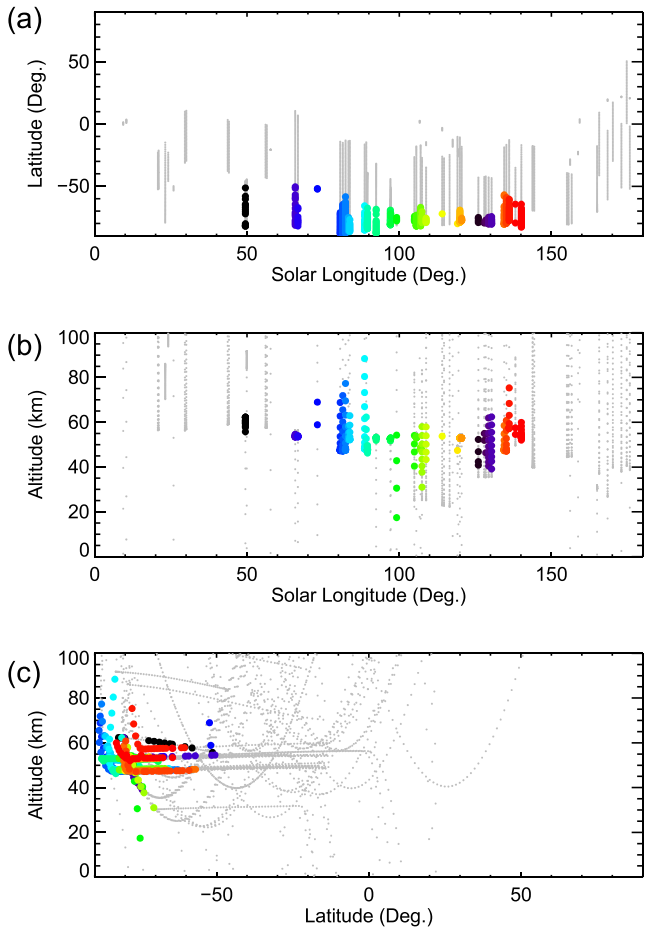

Figure 3. Positive detections ($R > 0.34$) of the NO ultraviolet nightglow in the Mars atmosphere, between $L_S = 0$ and 180° and between 0 and 100 km (colored dots). The nightglow is mainly detected at high southern latitudes, for altitudes between ~40 and 80 km. Gray dots represent all the UVIS nightside observations collected between 0 and 100 km, without a clear signature of the NO nightglow. Detections are color coded according to orbit number (from black during MY 35 to red in MY 37). Note that colors are independent from those in Figure 1.

The following area with many NO detections is considered for this part of the study: from $L_S = 40$ to 140°, between 10 and 90 km, and from 50°S to 90°S. This restricted data set is made up of 415 positive detections of the NO nightglow that are distributed in altitude according to Figure 4a. Light blue represents all the UVIS nightside limb observations matching these criteria, while dark blue represents the NO positive detections. The peaks at ~48 and ~52 km are associated with limb tracking observations at these altitudes that considerably increase the number of spectra acquired at those heights. The occurrence rate of the NO nightglow is illustrated in green in Figure 4b. It was calculated by dividing the dark blue histogram (positive detections) by the light blue one (all detections) of Figure 4a. The shape of the distribution is similar to that of the O_2 nightglow (Figure 2b) but slightly shifted to higher altitudes with an occurrence of 30% reached between 52 and 65 km. The high values below 40 km and above 65 km should be cautiously considered since it relies on a very limited sample of observations.

Figure 4c shows the brightness distribution of the NO nightglow ranging between 6 and 23 kR, with a mean value of 15 kR. These values agree with the limb measurements by Stiepen et al. (2017) acquired with the MAVEN/IUVS instrument. They found intensities ranging from 0.2 to 30 kR between 40 and 115 km. The map of the NO brightness in latitude-altitude coordinates is shown in Figure 4d. The altitude of the NO emitting layer cannot be clearly identified but seems to occur above 53 km, that is, at least 5 km above the O_2 visible nightglow layer.

3.3. Simultaneous O_2 and NO Detections

3.3.1. NOMAD/UVIS Observations

As previously explained, the strength of NOMAD/UVIS stands in its capability to simultaneously observe both the NO ultraviolet and the O_2 visible domains. An average nightside spectrum of all the simultaneous O_2 and NO detections is shown in Figure 5. This is the first time that these two nightside emissions can be observed simultaneously in the Martian atmosphere, an important constraint to understand the atmospheric dynamics of the Mars upper atmosphere. In this context, the altitude difference between the two emission layers is a key quantity.

Some NOMAD/UVIS orbits performed inertial limb observations and allow to almost instantaneously visualize this difference. Three of the best cases are illustrated in Figure 6. They correspond to orbits 17,797, 17,822 and 25,650. Red dots represent the O_2 limb brightness while NO intensities are shown with blue dots. Gray dots have been added as an indication of an upper limit brightness: no clear signature was found on these spectra and only a fit of the background noise could be calculated. Contrary to Figure 2d, these limb profiles allow to assess the O_2 emitting layer altitude: the emission peaks are observed at 49, 41 and 40 km, respectively. In these orbits, the O_2 emitting layer is always located below that of the NO by ~10 km (6, 12 and 14 km, respectively). The altitude difference is expected as the atomic oxygen and nitrogen densities peak at different altitudes and the excitation processes are different. The NO emitting layer is expected to occur where the product of the atomic oxygen and nitrogen densities is maximum. The N density usually peaking at ~90 km and the O density reaching its maximum around 60 km, the maximum of the product is reached between these altitudes. For the O_2 nightglow, the maximum brightness is proportional to the square of the O density multiplied by the CO_2 density. With the CO_2 density increasing when approaching the surface, the O_2 maximum brightness is expected to be located below 60 km.

Gérard et al. (2009) reached a similar conclusion about the NO δ and γ bands and the O_2 ($a^1\Delta_g$) infrared ~10 km difference of the emitting layer altitudes in the Venus atmosphere. On Mars, atoms are carried by the summer-to-winter circulation, while atoms are transported to the Venus night side through the subsolar-to-antisolar circulation. The Venus O_2 infrared nightglow is centered around the antisolar point (Soret et al., 2012), while the NO

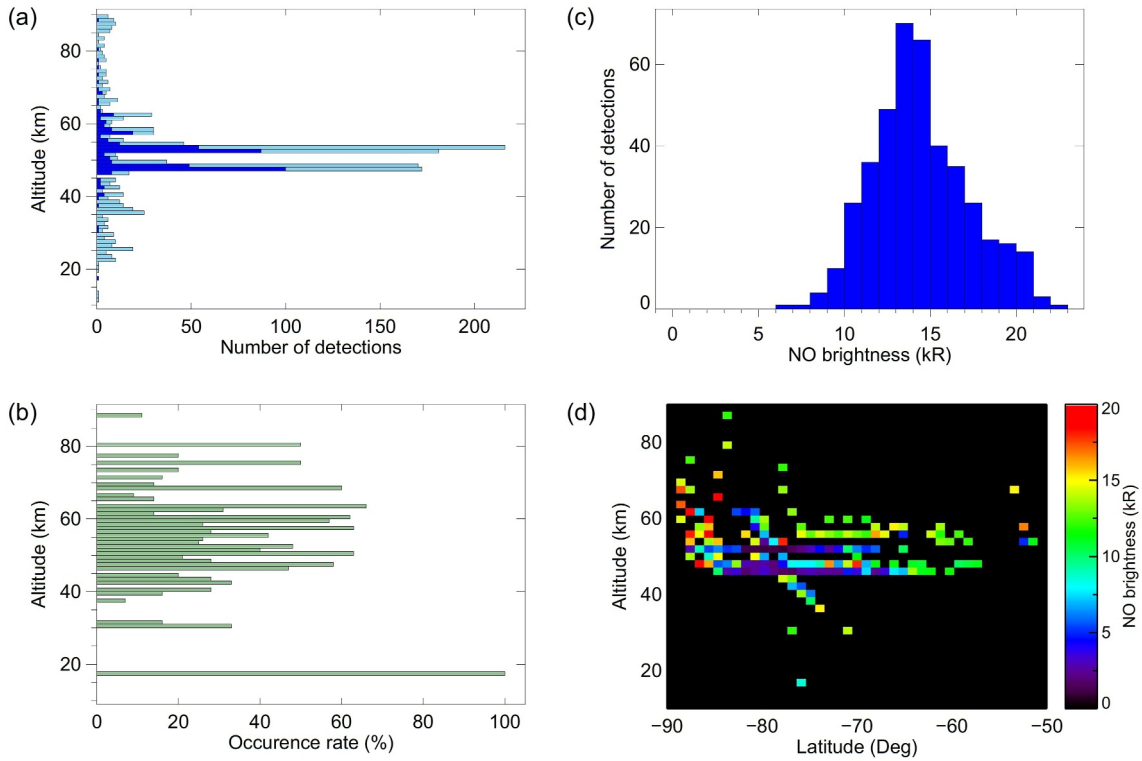

Figure 4. (a) Altitude distribution of the tangent point of the observations. Light blue represents all the UVIS observations matching the following criteria: SZA > 105°, solar longitude between 40° and 140°, between 10 and 90 km of altitude and between 50°S and 90°S. Dark blue represents positive NO detections ($R > 0.34$). (b) Occurrence rate of the NO altitude distribution. (c) Brightness distribution. (d) Latitude/altitude map of the NO brightness from NOMAD/UVIS nightside limb observations.

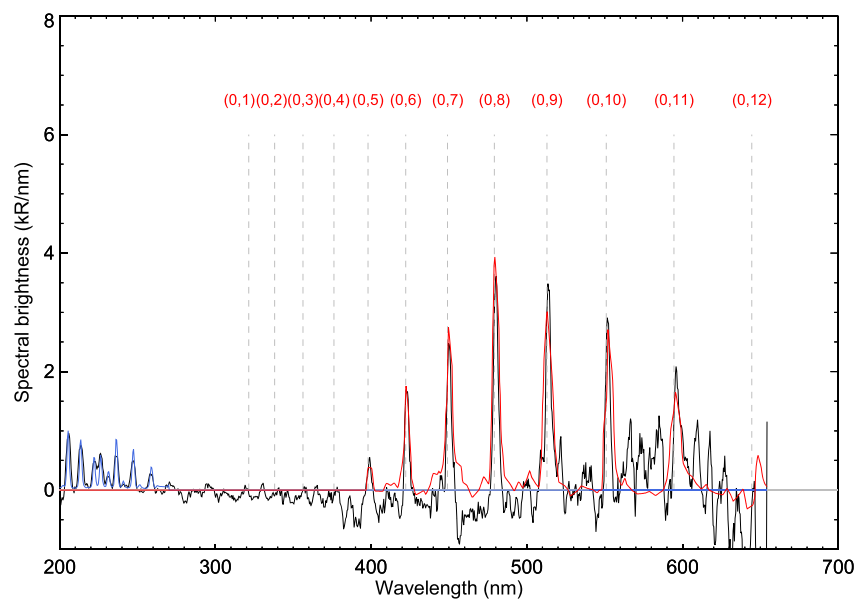

Figure 5. Average of 151 spectra with both NO and O_2 nightglow signatures (black). The blue spectrum corresponds to the MAVEN/IUVS NO reference spectrum (from Stiepen et al. (2017)). The red curve is the Venus reference spectrum for the O_2 nightglow (García Muñoz et al., 2009).

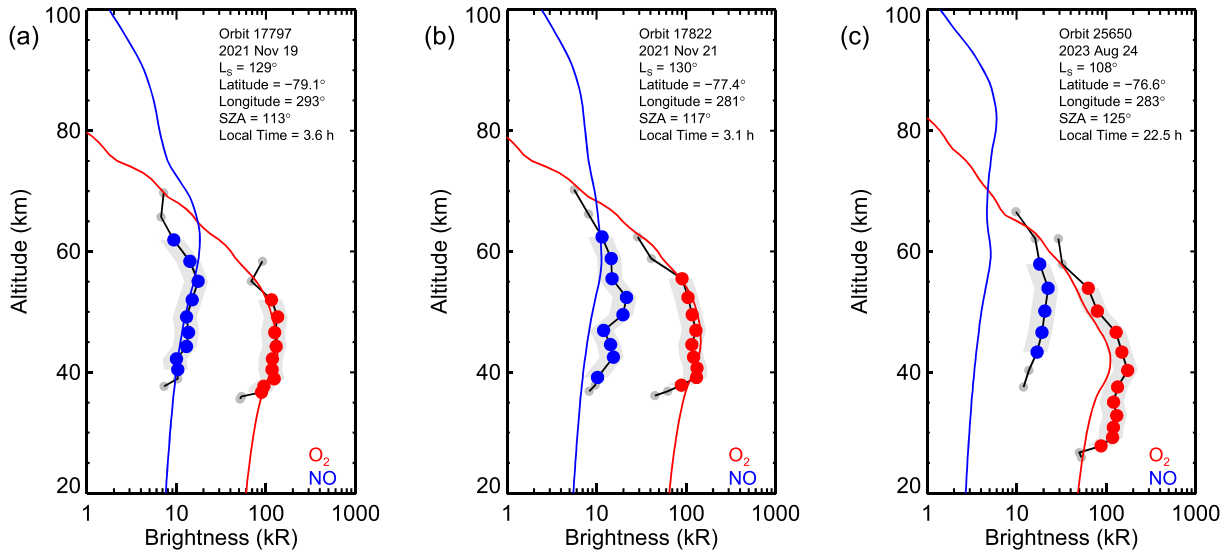

Figure 6. Dots represent NOMAD/UVIS observations. Colored lines represent model simulations with red for O_2 and blue for NO. Gray dots represent upper limit brightnesses in cases of non-detections. Simulations were performed at the indicated coordinates corresponding to the average coordinates of the O_2 and NO peak acquisition.

nightglow is shifted toward the morning hours (Stewart et al., 1980; Stiepen et al., 2013). A shift is neither expected nor observed in the present Martian study because all observations have been acquired near the southern pole, where local time is not a relevant parameter. On Venus, the emitting layers are located ∼55 km higher than those of the Mars atmosphere because of the different extent of their atmospheres. Bougher et al. (1990) showed that the altitude of the NO emitting layer occurs where the chemical destruction lifetime of N atoms equals that of the vertical transport, at ∼109 km. With a 2-D model, Collet et al. (2010) calculated a difference of 9–13 km (depending on the supply of atoms) between the NO and O_2 1.27 μm nightglow layers. Venus Express observations showed a mean difference of ∼15 km, with wide variations (Gérard et al., 2009). Brecht et al. (2021) showed that Kelvin and Rossby waves affect the atmospheric structure between 70 and 110 km and explain the Venus O_2 nightglow variability.

3.3.2. Three-Dimensional Simulations

We now use the M-PCM v6.1 (González-Galindo et al., 2013, 2015; Liu et al., 2023) to simulate those simultaneous nightglow emissions. While the model self-consistently simulates the NO nightglow and the O_2 ($a^1\Delta$) emissions, it does not include the possibility of simulating the O_2 Herzberg emission. The capacity to simulate this emission system from the O three-body recombination has now been incorporated into the model. The volume emission rates of the O_2 emissions are calculated as follows:

$$\eta_{O_2} = \varepsilon \times k \times [CO_2] \times [O]^2 \frac{A}{A + k_{CO_2} \times [CO_2] + k_O \times [O]} \quad (1)$$

with the effective yield for the production of the O $c^1\Sigma_u$ state $\varepsilon = 0.03$, the total transition probability of the c–X transition is $A = 0.17\ s^{-1}$, the quenching coefficients of the $c^1\Sigma_u$ state by CO_2 and O are respectively $k_{CO_2} = 3.1 \times 10^{-16}\ cm^{-3}\ s^{-1}$ and $k_O = 5.9 \times 10^{-12}\ cm^{-3}\ s^{-1}$ (Gérard et al., 2013; Krasnopolsky, 2011).

Simulations are shown in Figure 6 with blue and red solid curves for the NO and O_2 emissions, respectively. They are performed at the coordinates indicated in the figures. They correspond to the average coordinates of the O_2 and NO peak acquisitions. Orbits 17,797 and 17,822 occurred during MY36 and simulations rely on that same Martian year. However, orbit 25,650 took place during MY37, which is currently not available in the M-PCM model. Given that interannual variability of the dust load is not expected to be large around the aphelion season, we rely on MY36 simulations. At some other times of the Martian year, dust load could impact both the O_2 and NO nightglow emissions. More specifically, Gkouvelis et al. (2018, 2020) showed that a strong dust storm can level up the isobars and therefore increase the altitude of the nightglow layers.

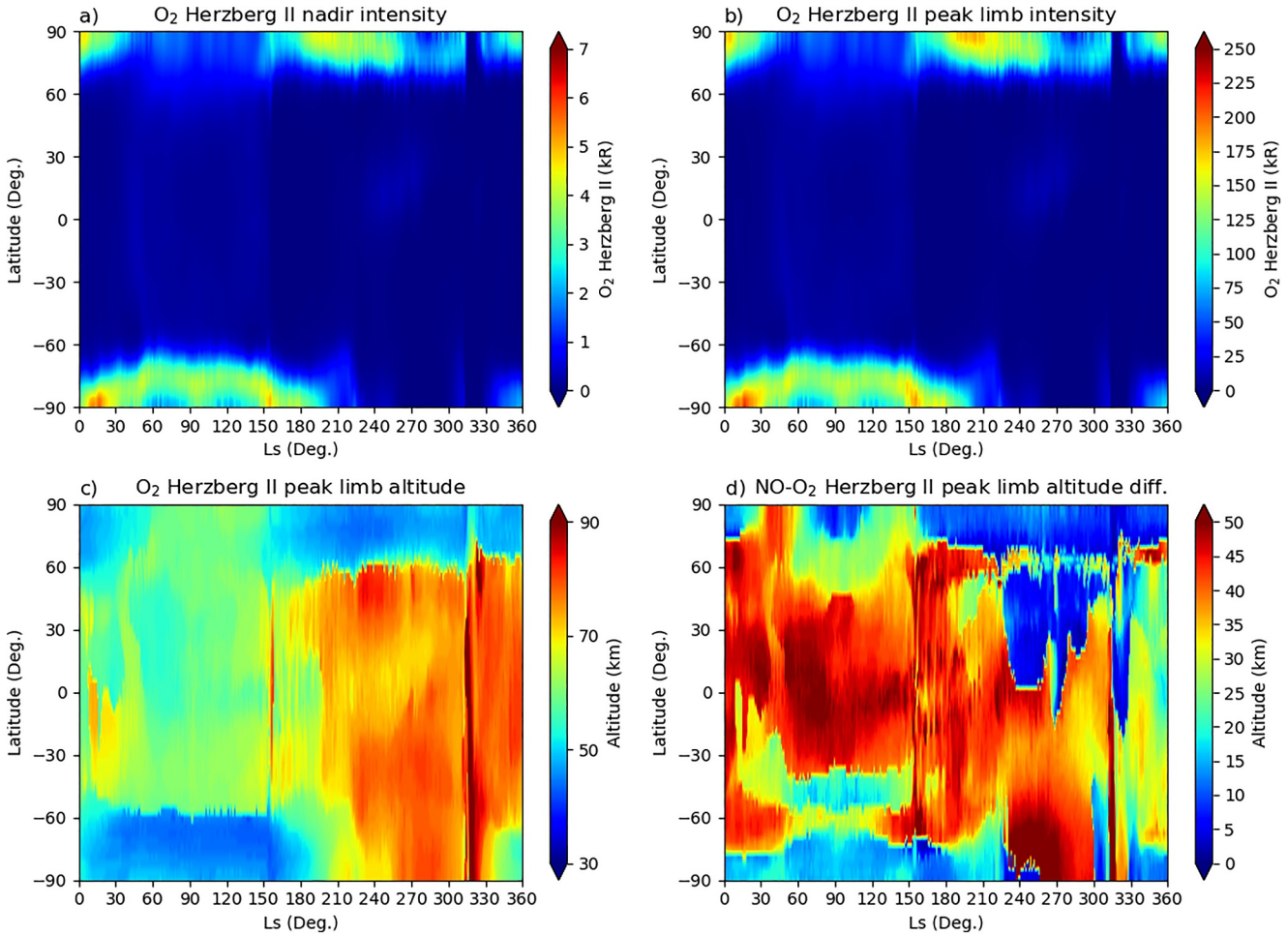

Figure 7. Maps of the simulated O_2 Herzberg II nadir brightness (a), peak limb intensity (b) and peak limb altitude (c). Map of the peak altitude difference between the NO and O_2 layers (d).

The agreement of the simulations with the UVIS observations of the O_2 nightglow is excellent, both in absolute brightness and altitude. The NO brightness is well reproduced for the first two cases but underestimated by a factor of four in the third case. The major difference for the 25,650 orbit with respect to orbits 17,797 and 17,822 is the local time. Observations during orbit 25,650 were made at 22:30 LT (dusk), while the other two have been acquired at 03:36 and 03:06 LT (dawn). A dawn/dusk asymmetry in the model could explain such a discrepancy. It is also possible that, due to the increasingly high solar activity during MY37, the N production rate by N_2 photodissociation is underestimated in the MY36 simulation analyzed here. Note also the different simulated NO profile shape for orbit 25,650, with two emission peaks, at 60 and 82 km. This seems related to the different altitude distributions of the O and N densities: O densities peak around 60 km and N densities at around 90 km, resulting in some cases, depending on the density ratio, in a double peak structure as the one simulated for this particular orbit. The simulated NO peak altitude is always overestimated by more than 10 km. This overestimation of the peak NO nightglow by the M-PCM has also been found in previous model-data comparisons (Stiepen et al., 2017). While we have explored different possibilities to eliminate or minimize this altitude difference, we currently have no definitive explanation for it.

The behavior of the Herzberg II bands during MY36 is illustrated in Figure 7. Figure 7a is a latitude-solar longitude map of the zonally averaged nadir O_2 nightglow brightness at a constant local time LT = 0 showing an abrupt enhancement at the winter poles. Figure 7b illustrates the peak limb brightness and shows a similar structure. These simulations corroborate the UVIS detections that have been observed between L_S 60 and 150°. The brightest O_2 emissions larger than a few tens of kR are however constrained in the model at higher latitudes

than ∼65°, while O_2 signatures of that magnitude were detected up to 50°S in the UVIS observations. The very faint intensities modeled in the equatorial regions explain why UVIS was not sensitive enough to detect any airglow signature at those latitudes.

While the overall structure of the simulated emission is similar to that presented in Figure 7b of Gagné et al. (2012) using a previous version of the M-PCM (LMD-MGCM), there are interesting differences. The brightest nadir Herzberg II emission in Gagné et al. (2012) also occurred at high winter latitudes, but was concentrated between 60° and 80° and did not reach the poles as in the current simulation. The simulated nadir brightness ranged from 3 to 5 kR in the southern hemisphere, which is ∼2 kR lower than the values shown in Figure 7a. Also, the northern hemisphere was about twice as bright as the southern hemisphere (reaching up to 8 kR), while the present M-PCM simulation does not predict the same asymmetry. The calculated emission at latitudes less than 50° ranged between 70 and 700 R. Their model also showed an abrupt transition between the two hemispheres near $L_S = 0°$ and 180°. The version of the M-PCM model used by Gagné et al. (2012) has significantly evolved since then. The main relevant differences that could impact the nightglow emissions include:

- The use of a unified photochemical scheme at all altitudes in the current version of the model (González-Galindo et al., 2009, 2013; Lefèvre et al., 2021) with respect to two separate photochemical models for the lower and upper atmosphere used in Gagné et al. (2012), allowing for a self-consistent calculation of both nightglow emissions using the same chemistry;
- The incorporation of an extended set of photochemical reactions, including ionospheric chemistry and additional chemical species (e.g., Chaufray et al., 2024), though their direct effect on the nightglow is not major;
- A better description of the water ice clouds and their radiative effects affecting the temperature distribution (Navarro et al., 2014);
- The incorporation of the thermal and dynamic effects of the deposition of momentum and energy by non-orographic gravity waves (Liu et al., 2023);
- A better vertical distribution of the dust load including the effects of rocket dust storms and the dust lifting produced by the flow over mountains (Lefèvre et al., 2021).

The last three improvements, though not directly related to the chemistry of the nightglow itself, affect the overall temperature and dynamics of the atmosphere predicted by the model, and have indirect effects on the simulated nightglow. For example, a modification of the temperature due to the radiative effects of the clouds or to a modified vertical distribution of the dust would affect the altitude of the nightglow layers; similarly, the modified dynamics due to the incorporation of the non-orographic gravity waves can affect the transport of species toward the poles and thus the distribution of the nightglow.

Note also that the rate coefficients used by Gagné et al. (2012) to calculate the O_2 Herzberg II brightness differ from those in Gérard et al. (2024) used in this simulation, and that different scenarios for the dust load and the UV solar flux resulting in N_2 and CO_2 photodissociation are used (solar average generic conditions and averaged dust climatology in Gagné et al. with respect to MY36 scenarios for both dust load and solar activity here).

The peak altitude of the Herzberg II emission represented in Figure 7c is lower near the poles than in the equatorial region. It also seems to be anticorrelated with the peak brightness. During southern winter, the simulated peak altitude of the O_2 visible emission is ∼50 km at the pole, in good agreement with the NOMAD/UVIS observations. Outside the bright winter polar regions, the O_2 intensity is very faint. The modeled peak altitude is however well defined and the altitude difference during the first and second part of the Martian year shown in Figure 7c is therefore reliable. It is interesting to note the increase in the peak altitude around $L_S = 320°$, corresponding to the presence of an intense dust storm on MY36 (see https://www-mars.lmd.jussieu.fr/mars/dust_climatology/index.html).

Figure 7d shows the altitude difference between the peak of the NO nightglow limb emission and that of the O_2 Herzberg II limb emission. The pattern is quite complex with abrupt changes due to the double-peaked structure of the NO nightglow mentioned above. The altitude difference can be as large as 50 km in the low to mid latitudes, depending on the season and latitude. Focusing on the polar regions, the predicted altitude difference is larger in the southern polar winter (differences between 10 and 20 km) than in the northern polar winter (usually values less than 10 km). Future observations with NOMAD in the northern winter could help to confirm or not this predicted behavior.

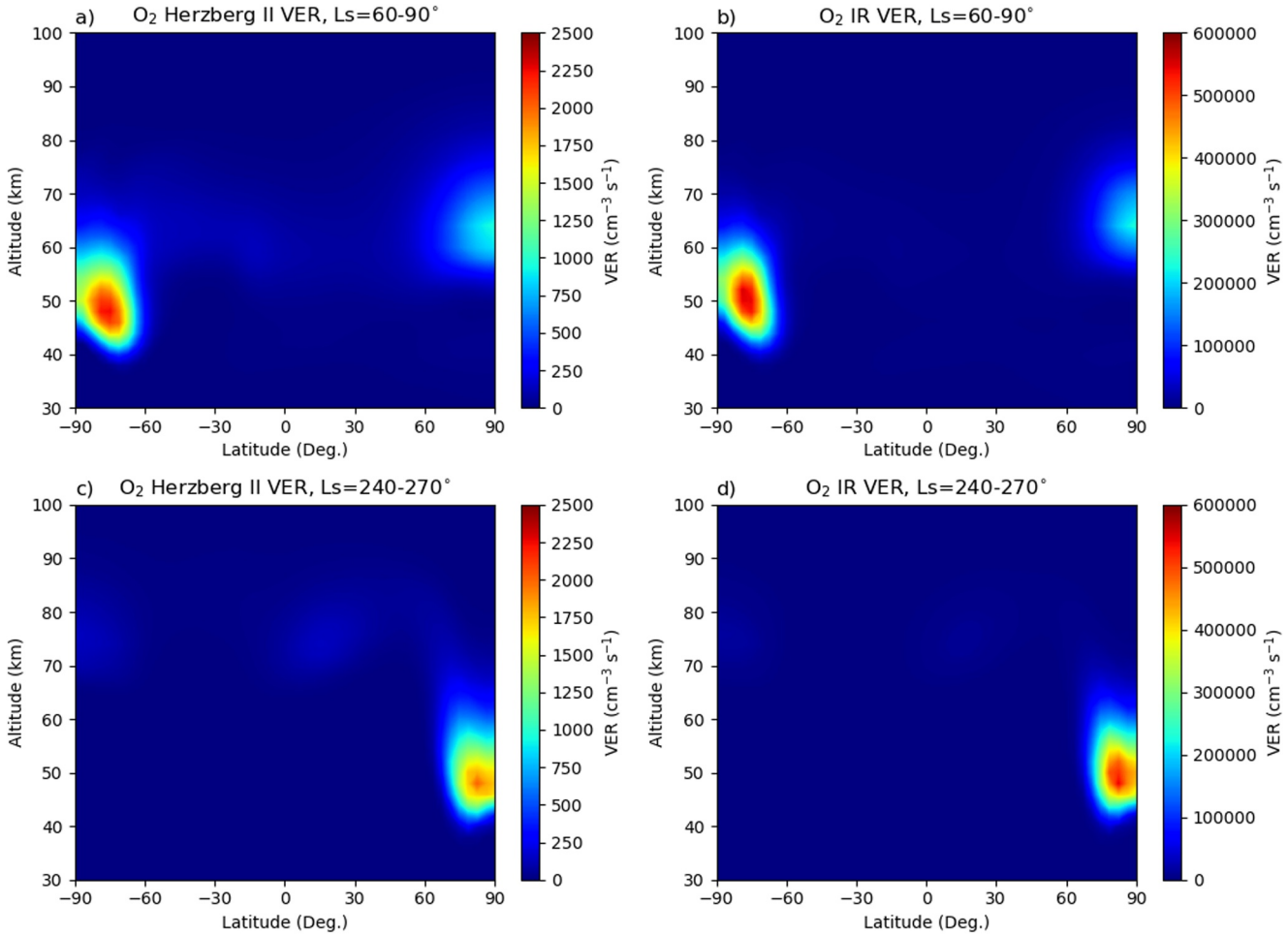

Figure 8. M-PCM simulations of the volume emission rates (VER) of the O_2 Herzberg II (left) and infrared at 1.27 μm (right) nightglow emissions during southern winter (L_S = 60–90°, top) and northern winter (L_S = 240–270°, bottom). The emissions are highly correlated and occur at high winter polar latitudes between 46 and 60 km.

3.4. The O_2 ($a^1\Delta_g$) Nightglow Emission

Section 3.3 is dedicated to the comparison of the O_2 visible and NO UV nightglow. The O_2 Herzberg II nightglow can also be compared to the O_2 ($a^1\Delta_g$) infrared nightglow at 1.27 μm. NOMAD is not able to observe in the IR, but this emission can be modeled. Krasnopolsky (2011) calculated the brightness of the Herzberg II and $a^1\Delta_g$ emissions to be 260 R and 12.6 kR, respectively, for the fall equinox at low latitude conditions. Using the former version of the M-PCM model, Gagné et al. (2012) found that $a^1\Delta_g$ is the most intense emission with a maximum intensity reaching over the poles during the solstice season. They showed seasonal-latitudinal plots of the O_2 ($a^1\Delta_g$) and Herzberg II nightglow emissions exhibiting a great deal of resemblance between the two emissions. Figure 8 considers the altitude of these oxygen emissions based on M-PCM simulations. For $a^1\Delta_g$, ε is taken equal to 0.75, the Einstein coefficient is $A = 2.2 \times 10^{-4}$ s^{-1}, the quenching coefficients by CO_2 and O are respectively $k_{CO_2} = 1 \times 10^{-20}$ cm^{-3} s^{-1} and $k_O = 2 \times 10^{-16}$ cm^{-3} s^{-1} (Gérard et al., 2013; Krasnopolsky, 2011). T is the temperature and the rate coefficient taken from Smith and Robertson (2008) is:

$$k = 7.5 \times 10^{-33} \times \left(\frac{T}{300}\right)^{-3.25} \quad (2)$$

As expected, both the visible and IR emissions occur at high winter polar latitudes (in the southern hemisphere at L_S = 90° and in the north at L_S = 270°). They also occur at almost the same altitude, with the peak of the 1.27 μm

emission being located ~2 km higher than the visible nightglow. The IR nightglow is ~240 times brighter than the visible emission. We therefore demonstrate that the Herzberg II and $a^1\Delta_g$ nightglow can equally be used to monitor the same region of the Mars upper atmosphere.

4. Conclusions

This study focuses on the first statistical results of the O_2 Herzberg II nightglow during the first half of the Martian year. This emission is bright enough to be detected during NOMAD/UVIS limb observations in the southern polar region. It is generated by the transport of O atoms produced in the sunlit summer polar region to the winter night polar region. The mean brightness is 108 kR and the emission layer is located between 40 and 50 km. The ultraviolet part of the NOMAD/UVIS spectra also allows to investigate the NO nightglow at high polar latitudes. Positive detections are located between 50 and 80 km with a mean brightness of 15 kR. Instantaneous visualization of the altitude difference between the ultraviolet and the visible layers in the UVIS limb observations shows that the NO nightglow occurs at higher altitudes (~10 km) than the O_2 emission. A similar conclusion was already reached for Venus. NO, O_2 ($a^1\Delta_g$) and Herzberg II nightglow emissions have also been simultaneously observed and their vertical and latitudinal distributions showed significant differences (Gérard et al., 2009, 2017). In the Venus case, the same photochemical processes as on Mars apply, but the atoms are transported through the subsolar-to-antisolar circulation.

We demonstrated that the M-PCM simulations correctly reproduced the O_2 nightglow both in brightness and altitude in the south polar region. As the O_2 Herzberg II production involves the square of the atomic oxygen density, we conclude that the atomic oxygen density is well calculated by the M-PCM model. However, simulations show that some model improvements must be performed to decrease the peak altitude of the NO nightglow. The NO nightglow being the product of the atomic oxygen and nitrogen densities, and the atomic oxygen density being well predicted by the model, it seems reasonable to incriminate the nitrogen density in the model, and in particular, its altitude distribution. Many sensitivity tests have been conducted, modifying chemical reaction rates and parameters governing the thermal balance in the mesosphere. However, none proved successful in bringing the model predicted altitude of the NO nightglow emission layer in agreement with the observations. Therefore, this discrepancy currently remains an open issue and deserves further investigation.

A comparison can also be made with Earth, where the Herzberg II system is very faint relative to Mars. This quasi-absence of the Herzberg II bands in the Earth's atmosphere stems from the particular role played by CO_2 as a third body in the recombination process. Unlike Mars and Venus, whose atmospheres are CO_2-dominated, the third body in the recombination process on Earth is mainly N_2. This difference explains the different relative intensities of the O_2 band systems on Earth and in CO_2-dominated atmospheres.

For this study, the data of the NOMAD/UVIS observational campaign were acquired during the first half of the Martian year. Therefore, due to the winter location of the NO and O_2 nightglow emissions, only the southern pole could be investigated. Future observations that will be performed in the north during the second part of the Martian year will confirm or not the simulated hemispheric asymmetry in the brightness and the altitude of the two emissions.

Finally, the aim of another study will be to derive the atomic oxygen density using inertial limb profiles of the molecular oxygen nightglow. Using this retrieved O density profile and simultaneous NO limb observations, the atomic nitrogen density will be derived as well. Such access to primary parameters will allow a direct comparison with Global Circulation Models to better investigate the source of discrepancies between data and model simulations.

Data Availability Statement

Data—Atmospheric temperature and densities from the Mars Climate Database are available from the 6.1 version of the MCD data at http://www-mars.lmd.jussieu.fr developed by Forget et al. (1999), Millour et al. (2018) and Gonzalez-Galindo et al. (2013). The NOMAD-UVIS spectra may be downloaded from ESA's PSA archives at https://archives.esac.esa.int/psa/#!Table%20View/NOMAD=instrument (select UVIS from the list of instruments and "Level 3 Calibrated" from the processing level). Data used in this study are available at Soret et al. (2024) with Creative Commons license CC BY 4.0.

Acknowledgments
The NOMAD experiment was led by the Royal Belgian Institute for Space Aeronomy (IASB-BIRA) with co-PI teams from Spain (IAA-CSIC), Italy (INAF-IAPS) and the United Kingdom (Open University). This project acknowledges funding by: the Belgian Science Policy Office (BELSPO) with the financial and contractual coordination by the ESA Prodex Office (PEA 4000103401, 4000121493, 4000140753, 4000140863); by the Spanish Ministry of Science and Innovation (MCIU) and European funds (Grants PGC2018-101836-B-I00 and ESP2017-87143-R; MINECO/FEDER), from the Severo Ochoa (CEX2021-001131-S) and from MCIN/AEI/10.13039/501100011033 (Grants PID2022-137579NB-I00, RTI2018-100920-J-I00 and PID2022-141216NB-I00); by the UK Space Agency (Grants ST/V002295/1, ST/V005332/1, ST/X006549/1, ST/Y000234/1 and ST/R003025/1); and by the Italian Space Agency (Grant 2018-2-HH.0). This work was supported by the Belgian Fonds de la Recherche Scientifique–FNRS (Grant 30442502; ET_HOME). L. S. and B. H. are supported by the Belgian Fund for Scientific Research (FNRS). We thank the ESA TGO team and its project scientists H. Svedhem and C. Wilson for supporting these observations.

References

Bertaux, J. L., Gondet, B., Lefèvre, F., Bibring, J. P., & Montmessin, F. (2012). First detection of O_2 1.27 μm nightglow emission at Mars with OMEGA/MEX and comparison with general circulation model predictions. *Journal of Geophysical Research*, *117*(E11). https://doi.org/10.1029/2011je003890

Bertaux, J. L., Leblanc, F., Perrier, S., Quemerais, E., Korablev, O., Dimarellis, E., et al. (2005). Nightglow in the upper atmosphere of Mars and implications for atmospheric transport. *Science*, *307*(5709), 566–569. https://doi.org/10.1126/science.1106957

Bougher, S. W., & Borucki, W. J. (1994). Venus O_2 visible and IR nightglow: Implications for lower thermosphere dynamics and chemistry. *Journal of Geophysical Research*, *99*(E2), 3759–3776. https://doi.org/10.1029/93je03431

Bougher, S. W., Gérard, J. C., Stewart, A. I. F., & Fesen, C. G. (1990). The Venus nitric oxide night airglow: Model calculations based on the Venus thermospheric general circulation model. *Journal of Geophysical Research*, *95*(A5), 6271–6284. https://doi.org/10.1029/JA095iA05p06271

Brecht, A. S., Bougher, S. W., Shields, D., Liu, H.-L., & Lee, C. (2021). Planetary-scale wave impacts on the Venusian upper mesosphere and lower thermosphere. *Journal of Geophysical Research: Planets*, *126*(1), e2020JE006587. https://doi.org/10.1029/2020JE006587

Chaufray, J.-Y., Gonzalez-Galindo, F., Leblanc, F., Modolo, R., Vals, M., Montmessin, F., et al. (2024). Simulations of the hydrogen and deuterium thermal and non-thermal escape at Mars at Spring Equinox. *Icarus*, *418*, 116152. https://doi.org/10.1016/j.icarus.2024.116152

Clancy, R. T., Sandor, B. J., Wolff, M. J., Smith, M. D., Lefèvre, F., Madeleine, J. B., et al. (2012). Extensive MRO CRISM observations of 1.27 μm O_2 airglow in Mars polar night and their comparison to MRO MCS temperature profiles and LMD GCM simulations. *Journal of Geophysical Research*, *117*(E11). https://doi.org/10.1029/2011je004018

Collet, A., Cox, C., & Gérard, J.-C. (2010). Two-dimensional time-dependent model of the transport of minor species in the Venus night side upper atmosphere. *Planetary and Space Science*, *58*(14–15), 1857–1867. https://doi.org/10.1016/j.pss.2010.08.016

Cox, C., Saglam, A., Gérard, J. C., Bertaux, J. L., González-Galindo, F., Leblanc, F., & Reberac, A. (2008). Distribution of the ultraviolet nitric oxide Martian night airglow: Observations from Mars Express and comparisons with a one-dimensional model. *Journal of Geophysical Research*, *113*(E8). https://doi.org/10.1029/2007je003037

Fedorova, A. A., Lefèvre, F., Guslyakova, S., Korablev, O., Bertaux, J. L., Montmessin, F., et al. (2012). The O_2 nightglow in the Martian atmosphere by SPICAM Onboard of Mars-Express. *Icarus*, *219*(2), 596–608. https://doi.org/10.1016/j.icarus.2012.03.031

Forget, F., Hourdin, F., Fournier, R., Hourdin, C., Talagrand, O., Collins, M., et al. (1999). Improved general circulation models of the Martianatmosphere from the surface to above 80 km. *Journal of Geophysical Research*, *104*(E10), 24155–24175. https://doi.org/10.1029/1999je001025

Gagné, M. È., Bertaux, J. L., González-Galindo, F., Melo, S. M., Montmessin, F., & Strong, K. (2013). New Nitric Oxide (NO) nightglow measurements with SPICAM/MEx as a tracer of Mars upper atmosphere circulation and comparison with LMD-MGCM model prediction: Evidence for asymmetric hemispheres. *Journal of Geophysical Research: Planets*, *118*(10), 2172–2179. https://doi.org/10.1002/jgre.20165

Gagné, M. È., Melo, S. M., Lefevre, F., González-Galindo, F., & Strong, K. (2012). Modeled O_2 airglow distributions in the Martian atmosphere. *Journal of Geophysical Research*, *117*(E6). https://doi.org/10.1029/2011je003901

García Muñoz, A., Mills, F. P., Slanger, T. G., Piccioni, G., & Drossart, P. (2009). Visible and near-infrared nightglow of molecular oxygen in the atmosphere of Venus. *Journal of Geophysical Research*, *114*(E12). https://doi.org/10.1029/2009je003447

Gérard, J. C., Bougher, S. W., López-Valverde, M. A., Pätzold, M., Drossart, P., & Piccioni, G. (2017). Aeronomy of the Venus upper atmosphere. *Space Science Reviews*, *212*(3–4), 1617–1683. https://doi.org/10.1007/s11214-017-0422-0

Gérard, J.-C., Cox, C., Soret, L., Saglam, A., Piccioni, G., Bertaux, J.-L., & Drossart, P. (2009). Concurrent observations of the ultraviolet nitric oxide and infrared O_2 nightglow emissions with Venus Express. *Journal of Geophysical Research*, *114*(E9), E00B44. https://doi.org/10.1029/2009JE003371

Gérard, J. C., Soret, L., Migliorini, A., & Piccioni, G. (2013). Oxygen nightglow emissions of Venus: Vertical distribution and collisional quenching. *Icarus*, *223*(1), 602–608. https://doi.org/10.1016/j.icarus.2012.11.019

Gérard, J. C., Soret, L., Thomas, I. R., Ristic, B., Willame, Y., Depiesse, C., et al. (2024). Observation of the Mars O_2 visible nightglow by the NOMAD spectrometer onboard the trace gas orbiter. *Nature Astronomy*, *8*(1), 77–81. https://doi.org/10.1038/s41550-023-02104-8

Gkouvelis, L., Gérard, J.-C., Ritter, B., Hubert, B., Schneider, N. M., & Jain, S. K. (2018). The O(^{1}S) 297.2-nm dayglow emission: A tracer of CO_2 density variations in the Martian lower thermosphere. *Journal of Geophysical Research: Planets*, *123*(12), 3119–3132. https://doi.org/10.1029/2018JE005709

Gkouvelis, L., Gérard, J.-C., Ritter, B., Hubert, B., Schneider, N. M., & Jain, S. K. (2020). Airglow remote sensing of the seasonal variation of the Martian upper atmosphere: MAVEN limb observations and model comparison. *Icarus*, *341*, 113666. https://doi.org/10.1016/j.icarus.2020.113666

González-Galindo, F., Chaufray, J.-Y., López-Valverde, M. A., Gilli, G., Forget, F., Leblanc, F., et al. (2013). Three-dimensional martianionosphere model: I. The photochemical ionosphere below 180 km. *Journal of Geophysical Research: Planets*, *118*(10), 2105–2123. https://doi.org/10.1002/jgre.20150

González-Galindo, F., Forget, F., López-Valverde, M. A., Angelats i Coll, M., & Millour, E. (2009). A ground-to-exosphere Martian general-circulation model: 1. Seasonal, diurnal, and solar cycle variation of thermospheric temperatures. *Journal of Geophysical Research*, *114*(E4), E04001. https://doi.org/10.1029/2008JE003246

González-Galindo, F., López-Valverde, M. A., Forget, F., García-Comas, M., Millour, E., & Montabone, L. (2015). Variability of the Martian thermosphere during eight Martian years as simulated by a ground-to-exosphere global circulation model. *Journal of Geophysical Research: Planets*, *120*(11), 2020–2035. https://doi.org/10.1002/2015JE004925

Krasnopolsky, V. A. (1983). *Venus spectroscopy in the 3000–8000 Å region by Veneras 9 and 10, in Venus*, (Ed.), D. M. Hunten, et al., The University of Arizona Press, pp. 459–483.

Krasnopolsky, V. A. (2011). Excitation of oxygen nightglow on the terrestrial planets. *Planetary and Space Science*, *59*(8), 754–766. https://doi.org/10.1016/j.pss.2011.02.015

Lefèvre, F., Lebonnois, S., Montmessin, F., & Forget, F. (2004). Three-dimensional modeling of ozone on Mars. *Journal of Geophysical Research*, *109*(E7), E07004. https://doi.org/10.1029/2004JE002268

Lefèvre, F., Trokhimovskiy, A., Fedorova, A., Baggio, L., Lacombe, G., Määttänen, A., et al. (2021). Relationship between the ozone and water Vapor columns on Mars as observed by SPICAM and calculated by a global climate model. *Journal of Geophysical Research: Planets*, *126*(4), e2021JE006838. https://doi.org/10.1029/2021JE006838

Liu, J., Millour, E., Forget, F., Gilli, G., Lott, F., Bardet, D., et al. (2023). A surface to exosphere non-orographic gravity wave parameterization for the Mars Planetary Climate Model. *Journal of Geophysical Research: Planets*, *128*(7), e2023JE007769. https://doi.org/10.1029/2023JE007769

Millour, E., Forget, F., Spiga, A., Pierron, T., Bierjon, A., Montabone, L., et al. (2022). The Mars climate database (version 6.1). In *Europlanet Science Congress 2022, Granada, Spain* (p. EPSC2022-786). https://doi.org/10.5194/epsc2022-786

Millour, E., Forget, F., Spiga, A., Vals, M., Zakharov, V., Montabone, L., et al. (2018). *The Mars climate database (version 5.3)*. ESAC.

Navarro, T., Madeleine, J. B., Forget, F., Spiga, A., Millour, E., Montmessin, F., & Määttänen, A. (2014). Global climate modeling of the Martian water cycle with improved microphysics and radiatively active water ice clouds. *Journal of Geophysical Research: Planets*, *119*(7), 1479–1495. https://doi.org/10.1002/2013JE004550

Patel, M. R., Antoine, P., Mason, J., Leese, M., Hathi, B., Stevens, A. H., et al. (2017). NOMAD spectrometer on the ExoMars trace gas orbiter mission: Part 2—Design, manufacturing, and testing of the ultraviolet and visible channel. *Applied Optics*, *56*(10), 2771–2782. https://doi.org/10.1364/AO.56.002771

Schneider, N. M., Milby, Z., Jain, S. K., González-Galindo, F., Royer, E., Gérard, J. C., et al. (2020). Imaging of Martian circulation patterns and atmospheric tides through MAVEN/IUVS nightglow observations. *Journal of Geophysical Research: Space Physics*, *125*(8), e2019JA027318. https://doi.org/10.1029/2019ja027318

Smith, G. P., & Robertson, R. (2008). Temperature dependence of oxygen atom recombination in nitrogen after ozone photolysis. *Chemical Physics Letters*, *458*(1–3), 6–10. https://doi.org/10.1016/j.cplett.2008.04.074

Soret, L., González-Galindo, F., Gérard, J.-C., Thomas, I., Ristic, B., Willame, Y., et al. (2024). Dataset for paper: "Ultraviolet NO and visible O_2 nightglow in the Mars southern winter polar region: Statistical study and model comparison [Dataset]. *ULiège Open Data Repository*. https://doi.org/10.58119/ULG/U19BNE

Soret, L., Gérard, J. C., Montmessin, F., Piccioni, G., Drossart, P., & Bertaux, J. L. (2012). Atomic oxygen on the Venus nihtside: Global distribution deduced from airglow mapping. *Icarus*, *217*(2), 849–855. https://doi.org/10.1016/j.icarus.2011.03.034

Stewart, A. I. F., Gérard, J. C., Rusch, D. W., & Bougher, S. W. (1980). Morphology of the Venus ultraviolet night airglow. *Journal of Geophysical Research*, *85*(A13), 7861–7870. https://doi.org/10.1029/ja085ia13p07861

Stiepen, A., Gérard, J.-C., Dumont, M., Cox, C., & Bertaux, J.-L. (2013). Venus nitric oxide nightglow mapping from SPICAV nadir observations. *Icarus*, *226*(1), 428–436. https://doi.org/10.1016/j.icarus.2013.05.031

Stiepen, A., Gérard, J. C., Gagné, M. È., Montmessin, F., & Bertaux, J. L. (2015). Ten years of Martian nitric oxide nightglow observations. *Geophysical Research Letters*, *42*(3), 720–725. https://doi.org/10.1002/2014gl062300

Stiepen, A., Jain, S. K., Schneider, N. M., Deighan, J. I., González-Galindo, F., Gérard, J. C., et al. (2017). Nitric oxide nightglow and Martian mesospheric circulation from MAVEN/IUVS observations and LMD-MGCM predictions. *Journal of Geophysical Research: Space Physics*, *122*(5), 5782–5797. https://doi.org/10.1002/2016JA023523

Vandaele, A. C., López-Moreno, J.-J., Patel, M. R., Bellucci, G., Daerden, F., Ristic, B., et al. (2018). NOMAD, an integrated suite of spectrometers for the ExoMars Trace Gas Mission: Technical description, science objectives, and expected performance. *Space Science Reviews*, *214*(5), 80. https://doi.org/10.1007/s11214-018-0517-2

Vandaele, A. C., Neefs, E., Drummond, R., Thomas, I. R., Daerden, F., López-Moreno, J. J., et al. (2018). Science objectives and performances of NOMAD, a spectrometer suite for the ExoMars TGO mission. *Planetary and Space Science*, *119*, 233–249. https://doi.org/10.1016/j.pss.2015.10.003

Willame, Y., Depiesse, C., Mason, J. P., Thomas, I. R., Patel, M. R., Hathi, B., et al. (2022). Calibration of the NOMAD-UVIS data. *Planetary and Space Science*, *218*, 105504. https://doi.org/10.1016/j.pss.2022.105504